An autoinhibited state of 53BP1 revealed by chemical probes and protein engineering

Gaofeng Cui[1,*], Maria Victoria Botuyan[1,*], Pascal Drané[2,*], Qi Hu[1], Benoît Bragantini[1], James R. Thompson[3], David J. Schuller[4], Michael T. Perfetti[5], Lindsey I. James[5,6], Stephen V. Frye[5,6], Dipanjan Chowdhury[2] and Georges Mer[1,7,#]

*Equal contributions

[#]Correspondence: mer.georges@mayo.edu

[1]Department of Biochemistry and Molecular Biology, Mayo Clinic, Rochester, MN, USA

[2]Department of Radiation Oncology, Dana-Farber Cancer Institute, Boston, MA, USA

[3]The Hormel Institute, University of Minnesota, Austin, MN, USA

[4]Cornell High Energy Synchrotron Source, Cornell University, Ithaca, NY, USA

[5]Center for Integrative Chemical Biology and Drug Discovery, Division of Chemical Biology and Medicinal Chemistry, UNC Eshelman School of Pharmacy, University of North Carolina at Chapel Hill, Chapel Hill, NC, USA

[6]Lineberger Comprehensive Cancer Center, University of North Carolina at Chapel Hill School of Medicine, Chapel Hill, NC, USA

[7]Department of Cancer Biology, Mayo Clinic, Rochester, MN, USA

Abstract

The recruitment of 53BP1 to chromatin, mediated by its recognition of histone H4 dimethylated at lysine 20 (H4K20me2), is important for DNA double-strand break repair. Using a series of small molecule antagonists, we demonstrate a conformational equilibrium between an open and a pre-existing lowly populated closed state of 53BP1 in which the H4K20me2 binding surface is buried at the interface between two interacting 53BP1 molecules. In cells, these antagonists inhibit the chromatin recruitment of wild type 53BP1, but do not affect 53BP1 variants unable to access the closed conformation despite preservation of the H4K20me2 binding site. Thus, this inhibition operates by shifting the conformational equilibrium toward the closed state. Our work therefore identifies an auto-associated form of 53BP1 — autoinhibited for chromatin binding — that can be stabilized by small molecule ligands encapsulated between two 53BP1 protomers. Such ligands are valuable chemical probes to reveal new aspects of 53BP1 mechanisms of action and have the potential to facilitate the development of new drugs for cancer therapy.

36 **Introduction**

37 The DNA damage response protein 53BP1 (p53-binding protein 1) influences the cell cycle
38 dependency of DNA double-strand break (DSB) repair pathway selection. During G1 phase of the cell
39 cycle, 53BP1 inactivates DSB repair by homologous recombination (HR) and promotes non-
40 homologous end joining (NHEJ). These activities are balanced by the BRCA1-BARD1 E3 ubiquitin
41 ligase, which promotes HR in post-replicative chromatin, possibly by reshuffling the chromatin
42 localization of 53BP1 during the S and G2 phases[1-3]. Both 53BP1 and BRCA1-BARD1 recognize
43 DSB-dependent mono-ubiquitylation of histone H2A K15 (H2AK15ub) in chromatin[4-9]. The
44 localization of 53BP1 to chromatin also requires that it binds histone H4 di-methylated at K20
45 (H4K20me2) via a tandem Tudor domain ($53BP1^{TT}$) [10,11], while BRCA1-BARD1 recruitment requires
46 unmethylated H4K20 recognized by an Ankyrin repeat domain in BARD1[8,9,12]. Our understanding of
47 how 53BP1 and BRCA1-BARD1 contribute to DNA repair pathway selection is incomplete.
48 Investigations of the antagonistic roles of 53BP1 and BRCA1-BARD1 have mostly relied on the
49 identification of separation-of-function mutations. Here, we explore the utility of small molecule
50 ligands that antagonize the recruitment of 53BP1 to chromatin. Blocking the H4K20me2 recognition
51 site of $53BP1^{TT}$ is a prospective means of preventing binding to chromatin. We show that a series of
52 water-soluble small molecules targeting the methyl-lysine binding cavity in $53BP1^{TT}$ function by
53 stabilizing a previously unknown lowly populated autoinhibited homodimeric state of $53BP1^{TT}$ in
54 which the histone binding surface of H4K20me2 is buried within the protomeric interface. Using these
55 small molecule antagonists and functional 53BP1 constructs consisting of both wild type and mutants
56 engineered to block auto-association via the tandem Tudor domain while retaining chromatin binding
57 capability, we then demonstrate that the autoinhibited state of 53BP1 exists in cells as well. This work
58 paves the way for further exploration of 53BP1 function and modes of action and provides insight for
59 the design of more potent and selective 53BP1 antagonists.

60

61 **Results**

62 **A 53BP1 tandem Tudor homodimer encapsulates small molecules in solution**

63 We previously identified a fragment-like small molecule, UNC2170, that binds the aromatic methyl-
64 lysine binding cage of $53BP1^{TT}$ with a dissociation constant (K_d) of 22 ± 2.5 μM and is competitive
65 with an H4K20me2 peptide[13]. Intriguingly, in a crystal structure of UNC2170 bound to $53BP1^{TT}$, the
66 small molecule ligand was in contact with two $53BP1^{TT}$ molecules. Our structural characterization of
67 $53BP1^{TT}$ in complex with the related compounds UNC2991 (K_d = 3.9 ± 0.4 μM), UNC3351 (K_d = 6.8
68 ± 0.4 μM) and UNC3474 (K_d = 1.0 ± 0.3 μM) (**Extended Data Fig. 1a)** revealed a similar three-
69 dimensional (3D) arrangement wherein each ligand not only blocked the methyl-lysine binding site but
70 was encapsulated in a cavity generated by two $53BP1^{TT}$ molecules (**Fig. 1a,b and Table 1**). This
71 consistent burial of the histone binding surface of $53BP1^{TT}$ by dimerization was unexpected. While
72 crystallization could drive $53BP1^{TT}$ homodimerization as has been shown for several other systems[14],
73 that all four 3D structures were comparable despite differing crystallization conditions and space
74 groups suggested that some $53BP1^{TT}$ dimer may also exist in solution, even though all previous NMR
75 spectroscopy studies only reported a monomeric state for $53BP1^{TT}$[10,11,15-17]. Since the
76 homodimerization interface in the crystal structures buries the histone binding surface of $53BP1^{TT}$,
77 such a conformation would be autoinhibitory for chromatin binding. Small molecules that stabilize this
78 autoinhibited state of $53BP1^{TT}$ — including in the context of full-length 53BP1 — could potentially
79 inhibit 53BP1 recruitment to DSBs.

80 Using analytical ultracentrifugation (AUC) sedimentation velocity, we showed that addition of
81 UNC3474 to $53BP1^{TT}$ caused a change in sedimentation coefficient that was consistent with the
82 dimerization of $53BP1^{TT}$ (**Fig. 2a**). Moreover, changes in small-angle X-ray scattering (SAXS) [18] data

upon 53BP1^{TT}-UNC3474 complex formation agreed well with 53BP1^{TT} homodimerization, including an increase in the radius of gyration (**Extended data Fig. 1b**). As a control, we used the small molecule UNC1118, which interacts with 53BP1^{TT} via a dimethyl-lysine-mimicking pyrrolidine-piperidine motif (IC_{50} = 7.4 ± 1.1 μM) as we previously showed[19]. We confirmed this interaction by measuring a K_d of 8.5 ± 0.9 μM (**Extended data Fig. 1c**). We hypothesized that UNC1118 would be too large to be buried within a 53BP1^{TT} homodimer. Addition of UNC1118 produced SAXS data similar to those of 53BP1^{TT} alone, indicating that UNC1118 is not capable of binding the homodimer (**Extended data Fig. 1b**). *Ab initio* derivation of molecular envelopes from the SAXS scattering curves of 53BP1^{TT} and 53BP1^{TT}-UNC3474 disclosed changes consistent with 53BP1^{TT} homodimerization in the presence of UNC3474 (**Extended data Fig. 1b**).

Investigation by solution NMR spectroscopy also revealed the dimeric conformation first identified in our 53BP1^{TT} crystal structures. Titration of UNC2170, UNC2991, UNC3351 and UNC3474 into ^{15}N-labeled 53BP1^{TT} led to changes in several signal positions in the ^{1}H-^{15}N heteronuclear single quantum coherence (HSQC) NMR spectrum of 53BP1^{TT} indicative of slow exchange on the chemical shift time scale (**Extended data Fig. 2a**). These chemical shift perturbations were more extensive than could be expected for just the small molecule binding surface and also mapped to amino acids located at the 53BP1^{TT} dimer interface in our crystal structures (**Extended data Fig. 2b,c**). Several of the 53BP1^{TT} residues that are close to the small molecule binding site had two different NMR signals. This is consistent with loss of symmetry observed in our crystal structures, allowing interactions by each of the two 53BP1^{TT} protomers with a different "side" of the bound small molecule (**Fig. 2b, Extended data Fig. 2b**). NMR relaxation data further supported an increase in molecular weight consistent with 53BP1^{TT} dimerization in the presence of UNC3474 as can be seen from an increase in R2 relaxation rates for the 53BP1^{TT}-UNC3474 complex (**Extended data Fig. 3a**). In comparison, binding of UNC1118 to 53BP1^{TT} had no marked effect on the relaxation rates of

107 53BP1^{TT} (**Extended data Fig. 3a**).

108 In addition, for the lowest affinity compound, UNC2170, we could quantify a slow exchange
109 between each of the two protomers in the 53BP1^{TT} dimer with interconversion rates of 1.7 s^{-1} and 1.2 s^{-}
110 ^{1} at 25 °C using 2D longitudinal ^{1}H-^{15}N-heteronuclear ZZ-exchange NMR spectroscopy[20-22] (**Fig. 2c**).
111 This exchange likely reflects the interconversion between the two 53BP1^{TT} protomers binding the two
112 different "sides" of the ligand. In the presence of the other compounds, which have higher affinity than
113 UNC2170 for 53BP1^{TT}, the exchange between the two 53BP1^{TT} protomers was too slow to be
114 quantifiable under the same conditions. Taken together, our data demonstrate that like in the crystal
115 structures, the small molecules are buried at the interface of a 53BP1^{TT} homodimer in solution.

116

117 **Identification of a weakly populated homodimeric state of 53BP1 tandem Tudor domain *in vitro***

118 The small molecules may cause 53BP1^{TT} to homodimerize or they could stabilize a weakly populated,
119 pre-existing 53BP1^{TT} homodimer that evaded prior detection. This distinction is important. If auto-
120 association, which buries the H4K20me2 binding surface in 53BP1^{TT}, also occurs in the context of
121 full-length 53BP1, then 53BP1 may employ autoinhibition as a regulatory mechanism for chromatin
122 recruitment.

123 In our crystal structures (**Fig. 1b**), W1495 of 53BP1^{TT} is essential for small molecule binding
124 and it also contributes to the 53BP1^{TT} homodimer interface. Several other inter-53BP1^{TT} contacts in
125 the crystal structures, however, are distant from the ligand binding site and might be exploited to
126 disrupt dimer formation while not affecting binding of the small molecules. Such inter-53BP1^{TT}
127 contacts include the hydrophobic interactions between Y1552 and L1518, and salt bridges involving
128 the E1549-R1583, D1550-R1490, and D1550-K1505 pairs (**Fig. 3a**). To test the possibility of a pre-
129 existing 53BP1^{TT} homodimer, we created a 53BP1^{TT} mutant (53BP1^{TT}-PN) in which E1549 and D1550

were replaced by a proline and an asparagine, respectively, to introduce a 3D structure-preserving β-turn in 53BP1^{TT}. These mutations eliminate the six salt bridges at the 53BP1^{TT} dimer interface as mentioned above but do not affect the small molecule-binding surface. We verified that the structural integrity of 53BP1^{TT}-PN was preserved by determining a 2.20 Å resolution crystal structure of this protein variant (**Fig. 3b, Table 1**). The backbone dynamic properties of wild type 53BP1^{TT} and 53BP1^{TT}-PN were quite similar as shown using NMR relaxation measurements (**Extended Data Fig. 3b**). Like wild type 53BP1^{TT}, 53BP1^{TT}-PN bound dimethylated histone (H4K20me2) and dimethylated p53 (p53K382me2) peptides as expected[10,11,16,17] (**Fig. 3c**), but unlike WT 53BP1^{TT}, 53BP1^{TT}-PN did not interact with UNC2170, UNC2991 or UNC3474 (**Fig. 3d**). There were no changes in the ^{1}H-^{15}N HSQC spectra of ^{15}N-labeled 53BP1^{TT}-PN after addition of up to 4-fold molar excess of each of these small molecules (**Fig. 3d**). As a control, we also examined the interaction of 53BP1^{TT}-PN with the compound UNC1078, which like UNC1118, is a larger molecule that interacts with 53BP1^{TT} as a monomer via an established dimethyl-lysine-mimicking pyrrolidine-piperidine motif and does not cause dimerization (**Extended Data Fig. 4a**). As expected, 53BP1^{TT}-PN also bound UNC1078 (**Fig. 3c**). The most likely interpretation for the absence of interaction of 53BP1^{TT}-PN with UNC2170, UNC2991 and UNC3474 is that these small molecules do not cause 53BP1^{TT} dimerization directly. Instead, they only bind to and stabilize a pre-existing 53BP1^{TT} homodimer population, shifting the equilibrium towards homodimer. When overlaid, the ^{1}H-^{15}N HSQC spectra of wild type 53BP1^{TT} and 53BP1^{TT}-PN showed small chemical shift changes that map to the inter-53BP1^{TT} interface in 53BP1^{TT}-UNC3474. This is further evidence for a preexisting small population of 53BP1^{TT} homodimer that is eliminated in 53BP1^{TT}-PN (**Extended Data Fig. 4b**).

As an added test of this binding mechanism, we designed a disulfide-crosslinked[23] 53BP1^{TT} variant that assembles into a stable dimer in the absence of a ligand. The replacement of E1549 and E1567 by cysteine residues readily linked two 53BP1^{TT} molecules covalently into a homodimer

154 (53BP1^{TT}-CC) via formation of two intermolecular C1549-C1567 disulfide bridges as shown using
155 AUC sedimentation velocity (**Fig. 4a**). A low resolution (3.8 Å) X-ray crystallography-based model of
156 53BP1^{TT}-CC was sufficient to demonstrate both protomers were arranged similarly as wild type
157 53BP1^{TT} bound to our small molecules with a backbone r.m.s.d. of 0.94 Å. (**Fig. 4b, Table 1**). Using
158 NMR spectroscopy, we independently verified that 53BP1^{TT}-CC mimicked the homodimeric state of
159 53BP1^{TT} bound to UNC3474 (**Fig. 4c**). Noticeably, the addition of UNC3474 led to the splitting of
160 several NMR signals in the ^{1}H-^{15}N HSQC spectra of 53BP1^{TT}-CC. Addition of the reducing agent
161 dithiothreitol (DTT) changed 53BP1^{TT}-CC to a monomeric state as expected which, like 53BP1^{TT}-PN,
162 had no affinity for UNC3474 (**Fig. 4c**). We therefore created 53BP1^{TT} variants that can be switched on
163 and off *in vitro* for ligand binding. These mutations may be useful for the study of a longer, functional
164 53BP1 in cells.

165

166 **Demonstration of an autoinhibited state of 53BP1 in cells using a chemical probe**

167 After showing that an autoinhibited state of 53BP1 exists *in vitro* and can be stabilized by small
168 molecules, we next evaluated the effect of these small molecules on 53BP1 localization to chromatin in
169 cells in response to DNA damage. We first reconstituted mammalian U2OS cell lines to stably express
170 a minimal segment of 53BP1 protein — the oligomeric foci-forming region (53BP1^{FFR}: residues 1220-
171 1711) — that contains the tandem Tudor domain and is necessary for DNA damage site recruitment[5,24-
172 26] (**Fig. 5a**). Cells were generated that express wild type (WT) 53BP1^{FFR} and the mutants 53BP1^{FFR}-PN
173 and 53BP1^{FFR}-CC.

174 Using immunofluorescence microscopy, we observed robust formation of ionizing radiation-
175 induced foci (IRIF) after cell exposure to 1 Gy of X-ray radiation for WT 53BP1^{FFR}, 53BP1^{FFR}-PN and
176 53BP1^{FFR}-CC (**Fig. 5b**). Upon treatment with different concentrations of UNC3474, IRIF formation
177 was inhibited in a dose-dependent manner for WT 53BP1^{FFR} (**Fig. 5b,c**). The Ser139-phosphorylated

178 histone H2A.X (γH2A.X) IRIF served as a marker for DNA damage in these experiments (**Fig. 5d**).
179 Under identical experimental conditions, there was no significant change in 53BP1^{FFR}-PN and
180 53BP1^{FFR}-CC IRIF upon treatment with UNC3474 (**Fig. 5c**). As we showed *in vitro*, 53BP1^{TT}-PN and
181 reduced-state 53BP1^{TT}-CC cannot dimerize and are thus insensitive to UNC3474 and to the related,
182 lower affinity compounds UNC2170 and UNC2991 (**Fig. 3d**). Importantly, 53BP1^{FFR}-CC should be in
183 a reduced state within mammalian cells, and therefore would be predicted to behave like 53BP1^{FFR}-PN.
184 These results show that UNC3474 inhibits the recruitment of 53BP1 to DSBs by stabilizing a pre-
185 existing autoinhibited state of 53BP1 in cells. We have therefore demonstrated the existence of an
186 autoinhibited form of 53BP1 by using a chemical probe.

187

188 **Discussion**

189 Numerous proteins harbor a methyl-lysine binding cage like that of 53BP1[27], making the development
190 of ligands that are selective for a single methyl-lysine reader protein challenging[28]. Nevertheless, a few
191 selective ligands for methyl-lysine readers have been developed[29]. For example, UNC1215 is a
192 bivalent chemical probe that potently binds chromatin-interacting transcriptional repressor L3MBTL3
193 by inducing the formation of a 2:2 protein:ligand complex[30]. In a radically different mechanism,
194 UNC3474 and the structurally related small molecules we characterized here stabilize a pre-existing
195 auto-associated form of 53BP1^{TT} with a 2:1 protein:ligand stoichiometry. Our studies revealed that
196 these compounds bind the aromatic cage of 53BP1^{TT}, but only when 53BP1^{TT} homodimers exist. We
197 showed that 53BP1^{TT} constructs engineered to prevent auto-association — while preserving the ligand
198 binding cage — have no affinity for the small molecule ligands, and yet, they bind H4K20me2 and
199 p53K382me2 like wild type 53BP1^{TT}.

200 Using these small molecules as chemical probes, we demonstrated that a pre-existing
201 autoinhibited form of 53BP1 exists in cells. The function of autoinhibited 53BP1 is not yet understood.

202 Nevertheless, we can speculate that this state may be stabilized *in vivo* under certain conditions to
203 regulate the activity of 53BP1. We note that full-length 53BP1 and $53BP1^{FFR}$ are constitutive
204 homomultimers[31] via an oligomerization domain of unknown structure located upstream from the
205 tandem Tudor domain[32-35]. In the context of oligomeric $53BP1^{FFR}$, the auto-association of $53BP1^{TT}$ and
206 its stabilization by small molecule ligands reported here are likely amplified by the avidity effect,
207 providing a unique and highly specific means of inhibiting the interaction of 53BP1 with chromatin. In
208 future studies, we will explore the influence of these ligands on other functions of 53BP1 reliant upon
209 its interactions with the regulatory protein TIRR[25,34,36-38] and K382me2-carrying p53 tumor
210 suppressor[16,39]. Ligand-binding to 53BP1 is predicted to disrupt these interactions.

211 Our work is expected to facilitate the structure-based design of improved ligands that are more
212 potent in stabilizing the $53BP1^{TT}$ homodimer and in inhibiting 53BP1 in cells. Such molecules would
213 help further dissect aspects of 53BP1 modes of action. These molecules could also be used to promote
214 DNA repair by homologous recombination and thereby increase the effectiveness of genome editing
215 using CRISPR-Cas9 or related systems[40,41]. Furthermore, pharmacological inhibition of 53BP1 is of
216 interest for brain cancer therapy[42]. For example, silencing of the 53BP1 gene sensitizes glioma cells to
217 ionizing radiation by prolonging cell cycle arrest and increasing apoptosis[43]. The expression of 53BP1
218 is increased in temozolomide-resistant glioblastoma cells and depletion of 53BP1 increases the potency
219 of temozolomide against glioblastoma[44]. Potent and selective inhibitors of 53BP1 could therefore serve
220 as lead compounds for drug development.

221

222 **References**

223

224 1 Bunting, S. F. *et al.* 53BP1 inhibits homologous recombination in *Brca1*-deficient cells by

225 blocking resection of DNA breaks. *Cell* **141**, 243-254 (2010).

226 2 Bouwman, P. *et al.* 53BP1 loss rescues BRCA1 deficiency and is associated with triple-
227 negative and BRCA-mutated breast cancers. *Nat Struct Mol Biol* **17**, 688-695 (2010).

228 3 Densham, R. M. *et al.* Human BRCA1-BARD1 ubiquitin ligase activity counteracts chromatin
229 barriers to DNA resection. *Nat Struct Mol Biol* **23**, 647-655 (2016).

230 4 Mattiroli, F. & Penengo, L. Histone Ubiquitination: An Integrative Signaling Platform in
231 Genome Stability. *Trends Genet* **37**, 566-581 (2021).

232 5 Fradet-Turcotte, A. *et al.* 53BP1 is a reader of the DNA-damage-induced H2A Lys 15 ubiquitin
233 mark. *Nature* **499**, 50-54 (2013).

234 6 Wilson, M. D. *et al.* The structural basis of modified nucleosome recognition by 53BP1. *Nature*
235 **536**, 100-103 (2016).

236 7 Becker, J. R. *et al.* BARD1 reads H2A lysine 15 ubiquitination to direct homologous
237 recombination. *Nature* **596**, 433-437 (2021).

238 8 Hu, Q. *et al.* Mechanisms of BRCA1-BARD1 nucleosome recognition and ubiquitylation.
239 *Nature* **596**, 438-443 (2021).

240 9 Dai, L. *et al.* Structural insight into BRCA1-BARD1 complex recruitment to damaged
241 chromatin. *Mol Cell* **81**, 2765-2777 e2766 (2021).

242 10 Botuyan, M. V. *et al.* Structural basis for the methylation state-specific recognition of histone
243 H4-K20 by 53BP1 and Crb2 in DNA repair. *Cell* **127**, 1361-1373 (2006).

244 11 Tang, J. *et al.* Acetylation limits 53BP1 association with damaged chromatin to promote
245 homologous recombination. *Nat Struct Mol Biol* **20**, 317-325 (2013).

246 12 Nakamura, K. *et al.* H4K20me0 recognition by BRCA1-BARD1 directs homologous

247 recombination to sister chromatids. *Nat Cell Biol* **21**, 311-318 (2019).

248 13 Perfetti, M. T. *et al.* Identification of a Fragment-like Small Molecule Ligand for the Methyl-
249 lysine Binding Protein, 53BP1. *ACS Chem Biol* **10**, 1072-1081 (2015).

250 14 Luo, J., Liu, Z., Guo, Y. & Li, M. A structural dissection of large protein-protein crystal packing
251 contacts. *Sci Rep* **5**, 14214 (2015).

252 15 Charier, G. *et al.* The Tudor tandem of 53BP1: a new structural motif involved in DNA and
253 RG-rich peptide binding. *Structure* **12**, 1551-1562 (2004).

254 16 Tong, Q. *et al.* Structural plasticity of methyllysine recognition by the tandem tudor domain of
255 53BP1. *Structure* **23**, 312-321 (2015).

256 17 Roy, S. *et al.* Structural insight into p53 recognition by the 53BP1 tandem Tudor domain. *J Mol*
257 *Biol* **398**, 489-496 (2010).

258 18 Rambo, R. P. & Tainer, J. A. Super-resolution in solution X-ray scattering and its applications
259 to structural systems biology. *Annu Rev Biophys* **42**, 415-441 (2013).

260 19 James, L. I. *et al.* Small-molecule ligands of methyl-lysine binding proteins: optimization of
261 selectivity for L3MBTL3. *J Med Chem* **56**, 7358-7371 (2013).

262 20 Farrow, N. A., Zhang, O., Forman-Kay, J. D. & Kay, L. E. Comparison of the backbone
263 dynamics of a folded and an unfolded SH3 domain existing in equilibrium in aqueous buffer.
264 *Biochemistry* **34**, 868-878 (1995).

265 21 Tyler, R. C., Wieting, J. C., Peterson, F. C. & Volkman, B. F. Electrostatic optimization of the
266 conformational energy landscape in a metamorphic protein. *Biochemistry* **51**, 9067-9075
267 (2012).

268 22 Zhang, Y. *et al.* High pressure ZZ-exchange NMR reveals key features of protein folding

269 transition dtates. *J Am Chem Soc* **138**, 15260-15266 (2016).

270 23 Mer, G., Kellenberger, E. & Lefèvre, J. F. Alpha-helix mimicry of a beta-turn. *J Mol Biol* **281**,
271 235-240 (1998).

272 24 Iwabuchi, K. *et al.* Potential role for 53BP1 in DNA end-joining repair through direct
273 interaction with DNA. *J Biol Chem* **278**, 36487-36495 (2003).

274 25 Drané, P. *et al.* TIRR regulates 53BP1 by masking its histone methyl-lysine binding function.
275 *Nature* **543**, 211-216 (2017).

276 26 Dos Santos Passos, C., Choi, Y. S., Snow, C. D., Yao, T. & Cohen, R. E. Design of genetically
277 encoded sensors to detect nucleosome ubiquitination in live cells. *J Cell Biol* **220** (2021).

278 27 Maurer-Stroh, S. *et al.* The Tudor domain 'Royal Family': Tudor, plant Agenet, Chromo,
279 PWWP and MBT domains. *Trends Biochem Sci* **28**, 69-74 (2003).

280 28 Linhares, B. M., Grembecka, J. & Cierpicki, T. Targeting epigenetic protein-protein interactions
281 with small-molecule inhibitors. *Future Med Chem* **12**, 1305-1326 (2020).

282 29 Arrowsmith, C. H. & Schapira, M. Targeting non-bromodomain chromatin readers. *Nat Struct*
283 *Mol Biol* **26**, 863-869 (2019).

284 30 James, L. I. *et al.* Discovery of a chemical probe for the L3MBTL3 methyllysine reader
285 domain. *Nat Chem Biol* **9**, 184-191 (2013).

286 31 Adams, M. M. *et al.* 53BP1 oligomerization is independent of its methylation by PRMT1. *Cell*
287 *Cycle* **4**, 1854-1861 (2005).

288 32 Ward, I. *et al.* The tandem BRCT domain of 53BP1 is not required for its repair function. *J Biol*
289 *Chem* **281**, 38472-38477 (2006).

290 33 Zgheib, O., Pataky, K., Brugger, J. & Halazonetis, T. D. An oligomerized 53BP1 tudor domain

291 suffices for recognition of DNA double-strand breaks. *Mol Cell Biol* **29**, 1050-1058 (2009).

292 34 Botuyan, M. V. *et al.* Mechanism of 53BP1 activity regulation by RNA-binding TIRR and a
293 designer protein. *Nat Struct Mol Biol* **25**, 591-600 (2018).

294 35 Sundaravinayagam, D. *et al.* 53BP1 supports immunoglobulin class switch recombination
295 independently of its DNA double-strand break end protection function. *Cell Rep* **28**, 1389-1399
296 e1386 (2019).

297 36 Zhang, A., Peng, B., Huang, P., Chen, J. & Gong, Z. The p53-binding protein 1-Tudor-
298 interacting repair regulator complex participates in the DNA damage response. *J Biol Chem*
299 **292**, 6461-6467 (2017).

300 37 Dai, Y., Zhang, A., Shan, S., Gong, Z. & Zhou, Z. Structural basis for recognition of 53BP1
301 tandem Tudor domain by TIRR. *Nat Commun* **9**, 2123 (2018).

302 38 Wang, J. *et al.* Molecular basis for the inhibition of the methyl-lysine binding function of
303 53BP1 by TIRR. *Nat Commun* **9**, 2689 (2018).

304 39 Parnandi, N. *et al.* TIRR inhibits the 53BP1-p53 complex to alter cell-fate programs. *Mol Cell*
305 **81**, 2583-2595 (2021).

306 40 Canny, M. D. *et al.* Inhibition of 53BP1 favors homology-dependent DNA repair and increases
307 CRISPR-Cas9 genome-editing efficiency. *Nat Biotechnol* **36**, 95-102 (2018).

308 41 Nambiar, T. S. *et al.* Stimulation of CRISPR-mediated homology-directed repair by an
309 engineered RAD18 variant. *Nat Commun* **10**, 3395 (2019).

310 42 Maleki Dana, P., Sadoughi, F., Mirzaei, H., Asemi, Z. & Yousefi, B. DNA damage response and
311 repair in the development and treatment of brain tumors. *Eur J Pharmacol* **924**, 174957 (2022).

312 43 Squatrito, M., Vanoli, F., Schultz, N., Jasin, M. & Holland, E. C. 53BP1 is a haploinsufficient

313 tumor suppressor and protects cells from radiation response in glioma. *Cancer Res* **72**, 5250-
314 5260 (2012).

315 44 Zhang, T., Chai, J. & Chi, L. Induction Of XLF And 53BP1 Expression Is Associated With
316 Temozolomide Resistance In Glioblastoma Cells. *Onco Targets Ther* **12**, 10139-10151 (2019).

317 45 Cui, G., Botuyan, M. V. & Mer, G. Preparation of recombinant peptides with site- and degree-
318 specific lysine 13C-methylation. *Biochemistry* **48**, 3798-3800 (2009).

319 46 Mallette, F. A. *et al.* RNF8- and RNF168-dependent degradation of KDM4A/JMJD2A triggers
320 53BP1 recruitment to DNA damage sites. *EMBO J* **31**, 1865-1878 (2012).

321 47 Cui, G. *et al.* PHF20 is an effector protein of p53 double lysine methylation that stabilizes and
322 activates p53. *Nat Struct Mol Biol* **19**, 916-924 (2012).

323 48 Delaglio, F. *et al.* NMRPipe: a multidimensional spectral processing system based on UNIX
324 pipes. *J Biomol NMR* **6**, 277-293 (1995).

325 49 Johnson, B. A. & Blevins, R. A. NMRView: a computer program for visualization and analysis
326 of NMR data. *J Biomol NMR* **4**, 603-614 (1994).

327 50 Johnson, B. A. From Raw Data to Protein Backbone Chemical Shifts Using NMRFx Processing
328 and NMRViewJ Analysis. *Methods Mol Biol* **1688**, 257-310 (2018).

329 51 Ferentz, A. E. & Wagner, G. NMR spectroscopy: a multifaceted approach to macromolecular
330 structure. *Q Rev Biophys* **33**, 29-65 (2000).

331 52 Dayie, K. T., Wagner, G. & Lefèvre, J. F. Theory and practice of nuclear spin relaxation in
332 proteins. *Annu Rev Phys Chem* **47**, 243-282 (1996).

333 53 Emsley, P. & Cowtan, K. Coot: model-building tools for molecular graphics. *Acta Crystallogr*
334 *D Biol Crystallogr* **60**, 2126-2132 (2004).

335 54 Adams, P. D. *et al.* PHENIX: a comprehensive Python-based system for macromolecular
336 structure solution. *Acta Crystallogr D Biol Crystallogr* **66**, 213-221 (2010).

337 55 Goddard, T. D. *et al.* UCSF ChimeraX: Meeting modern challenges in visualization and
338 analysis. *Protein Sci* **27**, 14-25 (2018).

339 56 Petoukhov, M. V. *et al.* New developments in the ATSAS program package for small-angle
340 scattering data analysis. *J Appl Cryst* **45**, 342-350 (2012).

341 57 Franke, D. *et al.* ATSAS 2.8: a comprehensive data analysis suite for small-angle scattering
342 from macromolecular solutions. *J Appl Crystallogr* **50**, 1212-1225 (2017).

343 58 Guinier, A. & Fournet, G. *Small-angle scattering of X-rays*. (John Wiley and Sons, 1955).

344 59 Schuck, P. Size-distribution analysis of macromolecules by sedimentation velocity
345 ultracentrifugation and lamm equation modeling. *Biophys J* **78**, 1606-1619 (2000).

346

347 **Methods**

348 **Protein purification**

349 The tandem Tudor domain of 53BP1 ($53BP1^{TT}$, residues 1481-1603) was purified as previously
350 described[10]. The W1495A, E1549P/D1550N ($53BP1^{TT}$-PN) and E1549C/E1567C ($53BP1^{TT}$-CC)
351 mutants were similarly prepared. The p53K382me2 (residues 377-386) peptide was purchased from
352 GenScript while the $H4K_C20me2$ (residues 12-25) was prepared from expression in *E. coli* with
353 chemical installation of a dimethyl-lysine analog as previously reported[45-47]. The two peptides were
354 purified by reversed-phase chromatography using a preparative C18 column (Phenomenex).

355

356

357 **Preparation of small compounds**

358 The small molecule ligands UNC2170, UNC2991, UNC3351, and UNC3474 and control ligands
359 UNC1078 and UNC1118 were synthesized as described previously[13,19].

360

361 **Nuclear magnetic resonance (NMR) spectroscopy**

362 All NMR data were collected at 25 °C on a 700 MHz Bruker Avance III spectrometer equipped with a
363 cryoprobe. Data were processed and analyzed with NMRPipe[48] and NMRViewJ[49,50].

364 For the backbone resonance assignments of $53BP1^{TT}$ in the presence of UNC3474, we prepared
365 samples of 1 mM ^{15}N- and ^{15}N,^{13}C-labeled WT $53BP1^{TT}$ with 5-fold molar excess of non-labeled
366 UNC3474 in 25 mM sodium phosphate, pH 7.0, 100 mM NaCl, 1.5 mM NaN_3, 0.3 mM DSS, 90%
367 H_2O/10% D_2O. A series of standard NMR experiments including 2D ^{1}H-^{15}N HSQC and ^{1}H-^{13}C HSQC
368 and 3D HNCACB, CBCA(CO)NH, HNCO, HN(CA)CO, HBHA(CO)NH, ^{15}N-edited NOESY-HSQC
369 and ^{13}C-edited NOESY-HSQC were recorded[51].

370 To probe chemical shift perturbations, ^{1}H-^{15}N HSQC spectra were acquired on the following
371 samples: 0.2 mM ^{15}N-labeled $53BP1^{TT}$ WT and $53BP1^{TT}$-PN in 25 mM sodium phosphate, pH 7.0, 1.5
372 mM NaN_3, 0.3 mM DSS, 90% H_2O/10% D_2O free and incrementally titrated with various non-labeled
373 inhibitors (UNC1078, UNC1118, UNC2170, UNC2991, UNC3474), as well as with $H4K_C20me2$ and
374 p53K382me2 peptides. Chemical shift perturbations (Δδ) were calculated using the equation:

375 $$\Delta\delta = \sqrt{(\Delta N/5)^2 + (\Delta H)^2}$$

376 where ΔN and ΔH are the corresponding differences in ^{15}N and ^{1}H chemical shifts between the bound
377 and free forms of 53BP1.

378 The NMR relaxation measurements were carried out with 1 mM ^{15}N-labeled $53BP1^{TT}$,

379 53BP1^{TT}-PN, and ^{15}N-labeled 53BP1^{TT} in the presence of saturating amounts of UNC3474 and
380 UNC1118 in 25 mM sodium phosphate, pH 7.0, 100 mM NaCl, 1.5 mM NaN_3, 0.3 mM DSS, 90%
381 H_2O/10% D_2O using standard experiments[52]. The longitudinal and transverse ^{15}N relaxation rates R1
382 and R2, were collected with 12 and 14 data points, respectively, using corresponding delay times of 0.1
383 - 2 s and 4 -120 ms. The ^{15}N-(^{1}H) nuclear Overhauser ratios were obtained from a refence experiment
384 without proton irradiation and a steady-state experiment with proton irradiation for 3 s.

385 The protomer interconversion rates in the 53BP1^{TT}-UNC2970 complex were determined using
386 2D longitudinal ^{1}H-^{15}N-heteronuclear ZZ-exchange NMR spectroscopy[20-22]. For these experiments, a
387 series of 11 spectra were acquired with mixing times of 0, 100, 200, 300, 400, 500, 600, 700, 800, 900,
388 and 1000 ms in 25 mM sodium phosphate, pH 7.0, 100 mM NaCl, 1.5 mM NaN_3, 0.3 mM DSS, 90%
389 H_2O/10% D_2O. The interconversion rates were obtained from nonlinear fitting of auto peak and
390 exchange peak intensities accounting for two-site exchange and ^{15}N R1 relaxation using the equations
391 previously described for a two-state model[22].

392

393 **X-ray crystallography**

394 Crystals of 53BP1^{TT}-PN mutant (40 mg/mL) were obtained by the hanging drop vapor diffusion
395 method, mixing 1 μL of the sample in buffer 1 (50 mM sodium phosphate, pH 7.5, 50 mM NaCl) and 1
396 μL of the reservoir solution at 22 °C. Crystals of 53BP1^{TT} WT (40 mg/mL) in complex with 14 mM of
397 UNC3474, UNC3351, and UNC2991 molecules (all in buffer 1) and crystals of 53BP1^{TT}-CC mutant
398 (15 mg/mL) in buffer 3 (50 mM Tris-HCl, pH 7.0, 100 mM NaCl) were obtained similarly. The
399 reservoir solutions that produced crystals were: 1.5 M sodium/potassium phosphate, pH 6.0 (for free
400 53BP1^{TT}-PN); 2 M sodium formate, 0.1 M Bis-tris propane, pH 7.0 (for 53BP1^{TT}-UNC3474); 0.1 M
401 sodium citrate tribasic, pH 5.6, 1 M ammonium phosphate monobasic (for 53BP1^{TT}-UNC3351); 1 M
402 sodium formate, 0.1 M Bis-tris propane, pH 7.0 (for 53BP1^{TT}-UNC2991); and 0.1 M Bis-Tris, pH 6.5

403 (for 53BP1^{TT}-CC). Crystals of 53BP1^{TT}-CC were cryoprotected with 25% (w/v) xylitol. All other
404 crystals were cryo-protected with 30% (v/v) glycerol.

405 Diffraction data for 53BP1^{TT}-PN and 53BP1^{TT}-UNC2991 were collected at the Cornel High
406 Energy Synchrotron Source (beamline A1), while data for 53BP1^{TT}-UNC3474 (beamline 19-ID),
407 53BP1^{TT}-UNC3351 (beamline 19-ID), and 53BP1^{TT}-CC (beamline 19-BM) were collected at the
408 Advanced Photon Source at Argonne National Laboratory. Diffraction data were processed with
409 HKL2000. Phases were determined by molecular replacement using the crystal structure of 53BP1
410 tandem Tudor domain (PDB 2G3R[10]). Model building and refinement were carried out with COOT[53]
411 and PHENIX[54]. All molecular representations were prepared with ChimeraX[55].

412

413 **Small angle X-ray scattering (SAXS)**

414 SAXS measurements were performed at 10 °C and different concentrations (2, 4 and 6 mg/mL) of
415 53BP1^{TT} WT, free and in complex with 10-fold molar excess of UNC3474 or UNC1118, in buffer 2
416 (25 mM sodium phosphate, pH 7.5, 15 mM NaCl), as well as on control samples containing only the
417 small molecule in buffer 3. SAXS data were collected at the Lawrence Berkeley National Laboratory
418 SYBILS beamline 12.3.1 and analyzed using programs from the SAXS data analysis software ATSAS
419 (version 2.4.2) [56,57] including PRIMUS, GNOM, AUTOPOROD, GASBOR and CRYSOL. PRIMUS
420 (version 3.0) was used for initial data processing. Radii of gyration (R_g) were calculated using the
421 Guinier approximation[58]. Distance distribution functions P(r) and maximum particle dimensions were
422 computed using GNOM. Molecular volumes and weights were estimated using AUTOPOROD. *Ab*
423 *initio* reconstructions of molecular envelopes were done using GASBOR 2.3i. CRYSOL was used to
424 back calculate the scattering curves and determine the goodness of fit.

425

426 **Isothermal titration calorimetry (ITC)**

427 The ITC measurements were performed at 25 °C using a MicroCal iTC200 calorimeter. 53BP1^{TT} and
428 the small molecules (UNC2991, UNC3351, UNC3474) were in 50 mM Tris-HCl, pH 7.5, 50 mM
429 NaCl. In a typical run, 53BP1^{TT} was in the reaction cell at a concentration of 150 to 160 μM while the
430 small molecule, in the titration syringe at a concentration of 0.8 to 2 mM, was delivered as 2 μL
431 injections every 3 min. The titrations were paired with control experiments for heat of dilution. The
432 titration of 53BP1^{TT} with UNC1118 was performed using a MicroCal VP-ITC calorimeter. ITC data
433 were fitted to a one-site model using a Levenberg-Marquardt non-linear regression algorithm
434 programmed in the Origin 7.0 software.

435

436 **Sedimentation velocity analytical ultracentrifugation (AUC)**

437 The AUC experiments were performed at 20 °C in 20 mM sodium phosphate, pH 7.5, with 50 mM
438 NaCl. 53BP1^{TT} was at a concentration of 20 μM. Measurements were recorded on an Optima
439 analytical ultracentrifuge (Beckman Coulter) with an An-50 Ti analytical 8-place rotor using
440 absorbance detection at 280 nm. Sample-filled AUC cells assembled with 12-mm charcoal-filled Epon
441 centerpieces and quartz windows were subjected to 3 h of equilibration at 20 °C under vacuum prior to
442 initiating the experiments at 50,000 rpm with continuous data acquisition for 20 h (200 scans) at 20 °C.
443 The AUC data were analyzed with the c(s) model in SEDFIT[59] using a partial specific volume of
444 0.7335 mL/g.

445

446 **Cell biology**

447 The focus-forming region (FFR; residues 1220-1711) of wild type 53BP1 and mutants
448 E1549P/D1550N (53BP1^{FFR}-PN) and E1549C/E1566C (53BP1^{FFR}-CC) were inserted into the

449 retroviral vector POZ. The 53BP1^{FFR} constructs were stably expressed at a moderate level in U2OS
450 cells. To probe the effect of UNC3474 on 53BP1^{FFR} IRIF formation, U2OS cells were grown on glass
451 coverslips, pre-incubated for 1 h with various concentrations of UNC3474 inhibitor and exposed to 1
452 Gy of X-ray radiation. After 1 h, the cells were fixed in 4% formaldehyde in PBS for 15 min at room
453 temperature and blocked and permeabilized for 1 h in PBS containing 0.3% Triton X-100, 1% BSA,
454 10% fetal bovine. For immunofluorescence, 53BP1^{FFR} proteins (WT and 53BP1-PN) and γH2A.X
455 were stained respectively with HA-Tag (C29F4) rabbit antibody (Cell Signaling Technology) and anti-
456 γH2A.X (Ser139) (JBW301) mouse antibody (MilliporeSigma). Incubation with primary and
457 secondary antibodies (Alexa Fluor, Molecular Probes) were done in PBS containing 1% BSA and 0.1%
458 Triton X-100 for 1 h at room temperature. Coverslips were mounted using DAPI Fluoromount-G
459 (Southern Biotech).

460

461 **Data availability**

462 The crystal structures have been deposited in the Protein Data Bank under accession codes 6MXX
463 (53BP1^{TT}-UNC2991), 6MXY (53BP1^{TT}-UNC3351), 6MXZ (53BP1^{TT}-UNC3474), 6MY0 (53BP1^{TT}-
464 PN), and 8FKH (53BP1^{TT}-CC).

465

466 **Acknowledgements**

467 We are very grateful to Nicolas Foloppe for insightful discussions and advice, to Kemin Tan at Argonne
468 National Laboratory Advanced Photon Source (APS) for assistance with X-ray data collection and to Greg
469 Hura at Lawrence Berkeley National Laboratory Advanced Light Source (ALS) for assistance with
470 SAXS data collection. This research was supported by the US National Institutes of Health (NIH)
471 awards R35 GM136262 and R01 CA132878 to G.M., US Department of Defense Ovarian Cancer

Research Program awards W81XWH-16-1-0391 and W81XWH-20-1-0322 to M.V.B. and G.M., and NIH grants R01 CA208244 and R01 CA264900 and Gray Foundation Team Science Award to D.C. X-ray crystallography data were collected at the APS Structural Biology Center funded by the U.S. Department of Energy (DOE), Office of Biological and Environmental Research and operated for the DOE Office of Science by Argonne National Laboratory under contract DE-AC02-06CH11357. X-ray crystallography data were also collected at the Cornell High-Energy Synchrotron Source (CHESS), which is supported by the National Science Foundation under award DMR-1829070, and the Macromolecular Diffraction at CHESS (MacCHESS) facility, which is supported by NIH award P30 GM124166. The SAXS data were collected at the ALS SIBYLS beamline, supported by the DOE, Office of Biological Environmental Research, and by the NIH project ALS-ENABLE (P30 GM124169) and High-End Instrumentation Grant S10 OD018483.

Author contributions

Conceptualization, G.M., G. C., and M. V. B.; Investigation, G. C., M. V. B., P. D., Q. H., B. B., J. R. T., D. J. S., M. T. P., L. I. J., and G. M.; Writing—original draft, G. M. and M. V. B.; writing—review and editing, G. M., M. V. B., J. R. T., G. C., P. D., D. J. S., L. I. J., S. V. F., visualization, Q. H., B. B., and D. J. S.; G. C., P. D., Q. H., B. B., M. V. B., and G. M.; Supervision, G. M. and D. C.

Competing interests

The authors declare no competing interests.

495 **Figures and Legends**

496

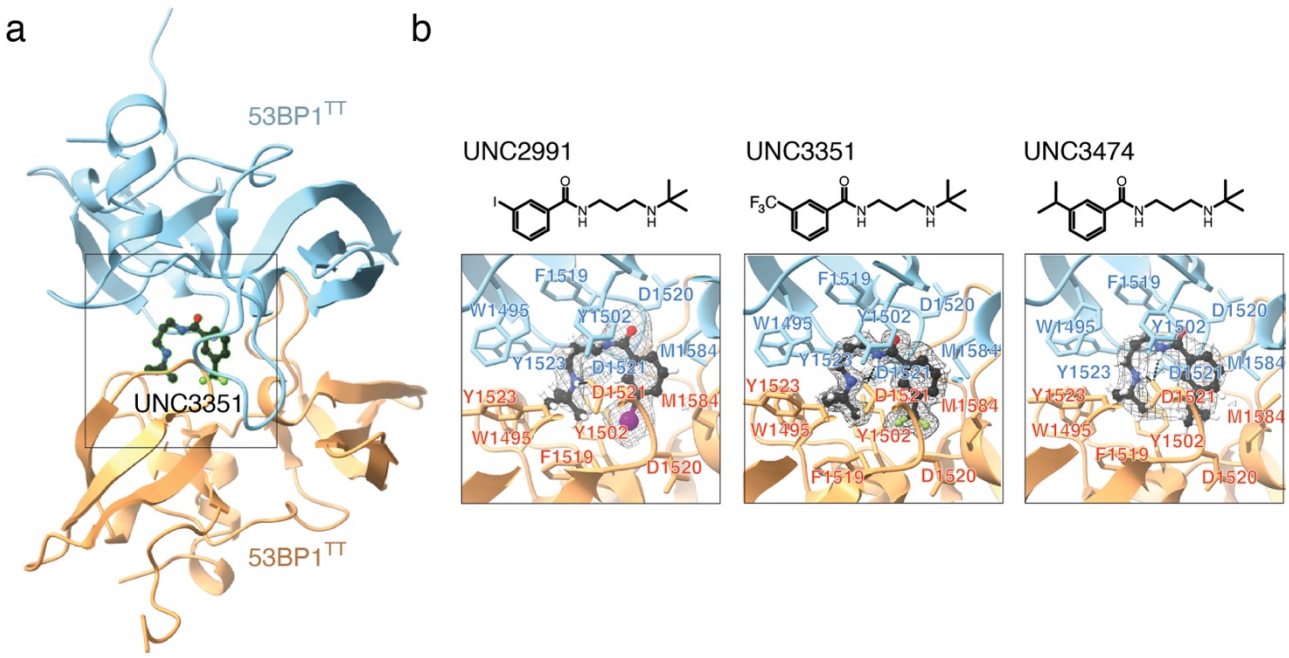

497

498 **Figure 1 | Interaction of 53BP1^{TT} with small molecules probed using X-ray crystallography.**

499 **a**, Crystal structure showing the encapsulation of UNC3351 by two 53BP1^{TT} molecules.

500 **b**, Binding interfaces of UNC2991, UNC3351 and UNC3474 with 53BP1^{TT} in the crystal structures of
501 their complexes. The 2mFo-DFc electron density maps, contoured at 1σ level, are shown as gray mesh
502 around each compound.

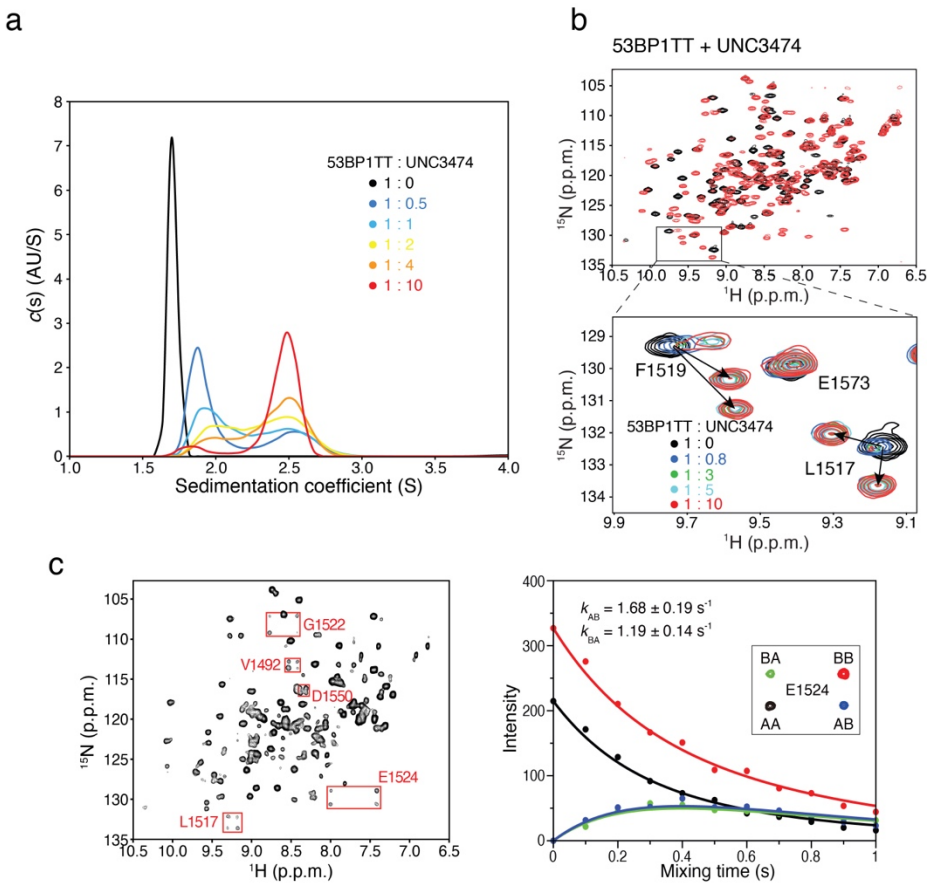

503

504 **Figure 2 | Oligomerization of 53BP1^{TT}-UNC3474 probed using analytical ultracentrifugation**

505 **(AUC) and NMR spectroscopy.**

506 **a**, Sedimentation velocity analysis of 53BP1^{TT} (20 μM) at different concentrations of UNC3474 using
507 AUC. The sedimentation coefficient distributions are shown for free 53BP1^{TT} (black) and for 53BP1^{TT}
508 at increasing concentrations of UNC3474; 10 μM (blue), 20 μM (light blue), 40 μM (yellow), 80 μM
509 (orange) and 200 μM (red).

510 **b**, Top: Overlay of ^{1}H-^{15}N HSQC NMR spectra of ^{15}N-labeled 53BP1^{TT}, free (black) and bound to
511 UNC3474 (red). Bottom: Examples of doubling of resonances (L1517 and F1519 signals) at different
512 53BP1^{TT}:UNC3474 molar ratios.

513 **c**. ^{1}H-^{15}N-heteronuclear ZZ-exchange NMR spectroscopy of the interaction of 53BP1^{TT} with
514 UNC2170 at 25 °C using 1 mM ^{15}N-labeled 53BP1^{TT} and 9 mM UNC2170. Fitting was done for the
515 signals of E1524 (inset). The black and red curves show the decay of the auto peaks (AA and BB) and
516 blue and green curves show the buildup and decay of the exchange peaks (AB and BA). The
517 interconversion rates are indicated.

518

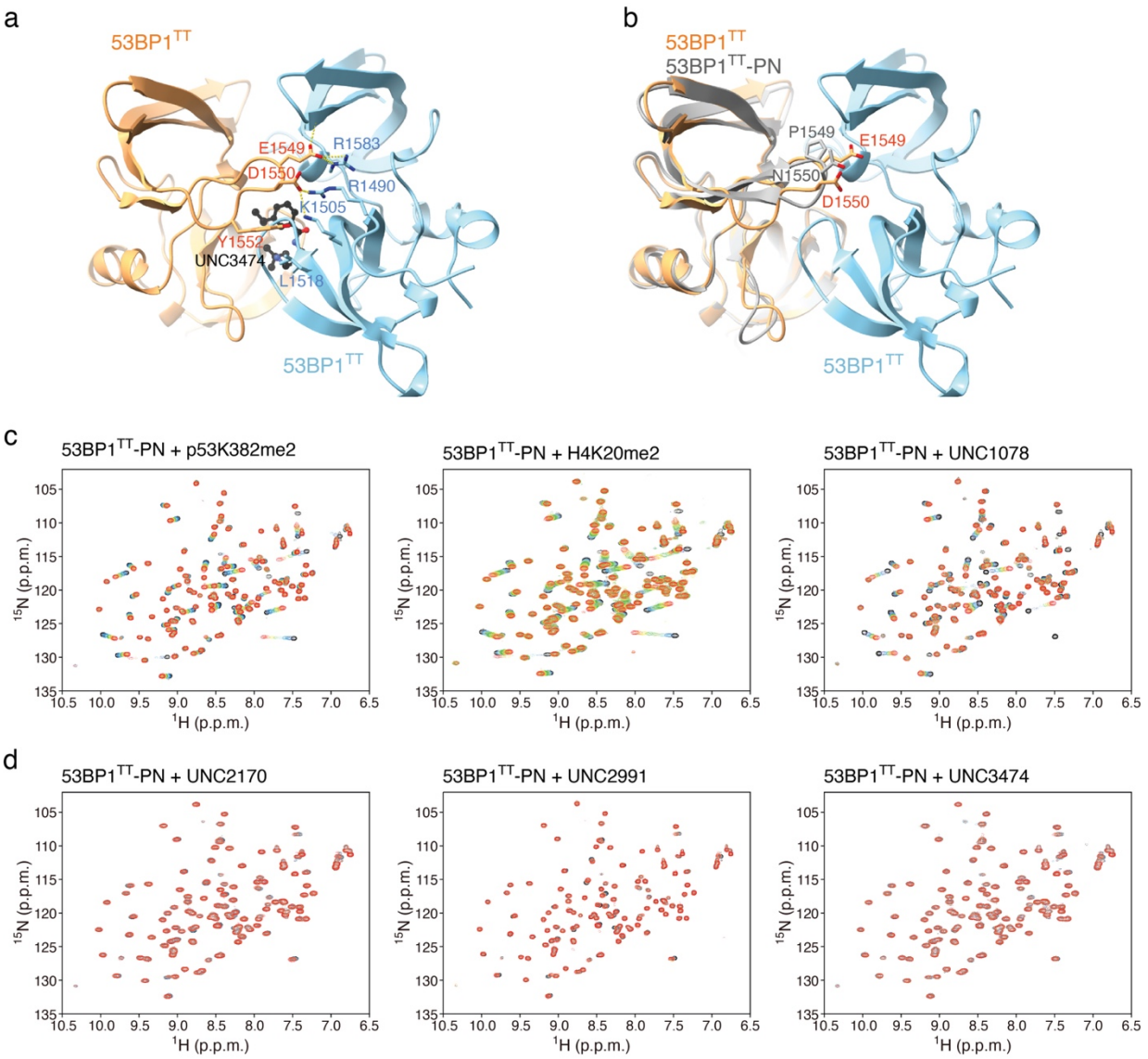

Figure 3 | Small molecules stabilize a pre-existing lowly populated 53BP1^{TT} homodimer.

a, Key inter-53BP1^{TT} contacts in the structure of 53BP1^{TT}-UNC3474 complex. Hydrogen bonds and salt bridges are represented by yellow dashed lines.

b, Structural overlay of wild type 53BP1^{TT} and mutant 53BP1^{TT}-PN in which E1549 and D1550 are replaced by a proline and an asparagine, respectively.

c, NMR spectroscopy-monitored titration of ^{15}N-labeled 53BP1^{TT}-PN with non-labeled H4K$_C$20me2 and p53K382me2 peptides and small molecule UNC1078. Shown in different colors are the overlaid ^{1}H-^{15}N HSQC spectra of 53BP1^{TT}-PN recorded without (black) and with increasing amounts of added compounds, up to 4-fold molar excess (red).

d, Same as **c** but for the titration of 53BP1^{TT}-PN with small molecules UNC2170, UNC2991 and UNC3474.

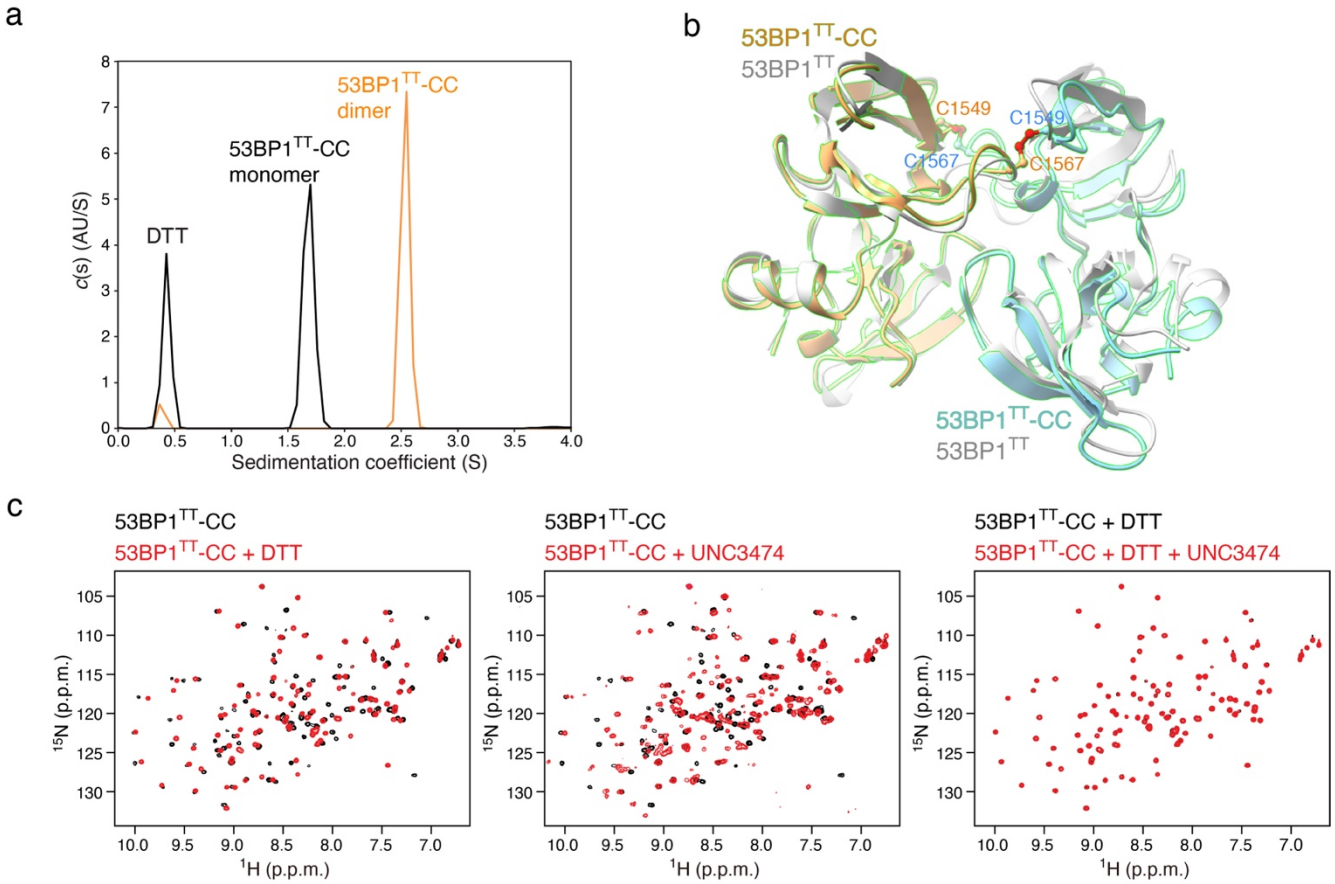

Figure 4 | Engineering of a disulfide-crosslinked 53BP1^{TT} homodimer that binds UNC3474.

a, Sedimentation velocity analysis of 53BP1^{TT}-CC (20 μM) in the presence and absence of 10 mM DTT.

b, Crystal structure of 53BP1^{TT}-CC (blue and orange) showing the two disulfide bridges overlaid to the crystal structure of 53BP1^{TT}-UNC3474 (UNC3474 omitted) in gray.

c, Effects of adding 2 mM DTT and UNC3474 on the ^{1}H-^{15}N HSQC spectrum of ^{15}N-labeled 53BP1^{TT}-CC (1:1 UNC3474:53BP1^{TT}-CC molar ratio).

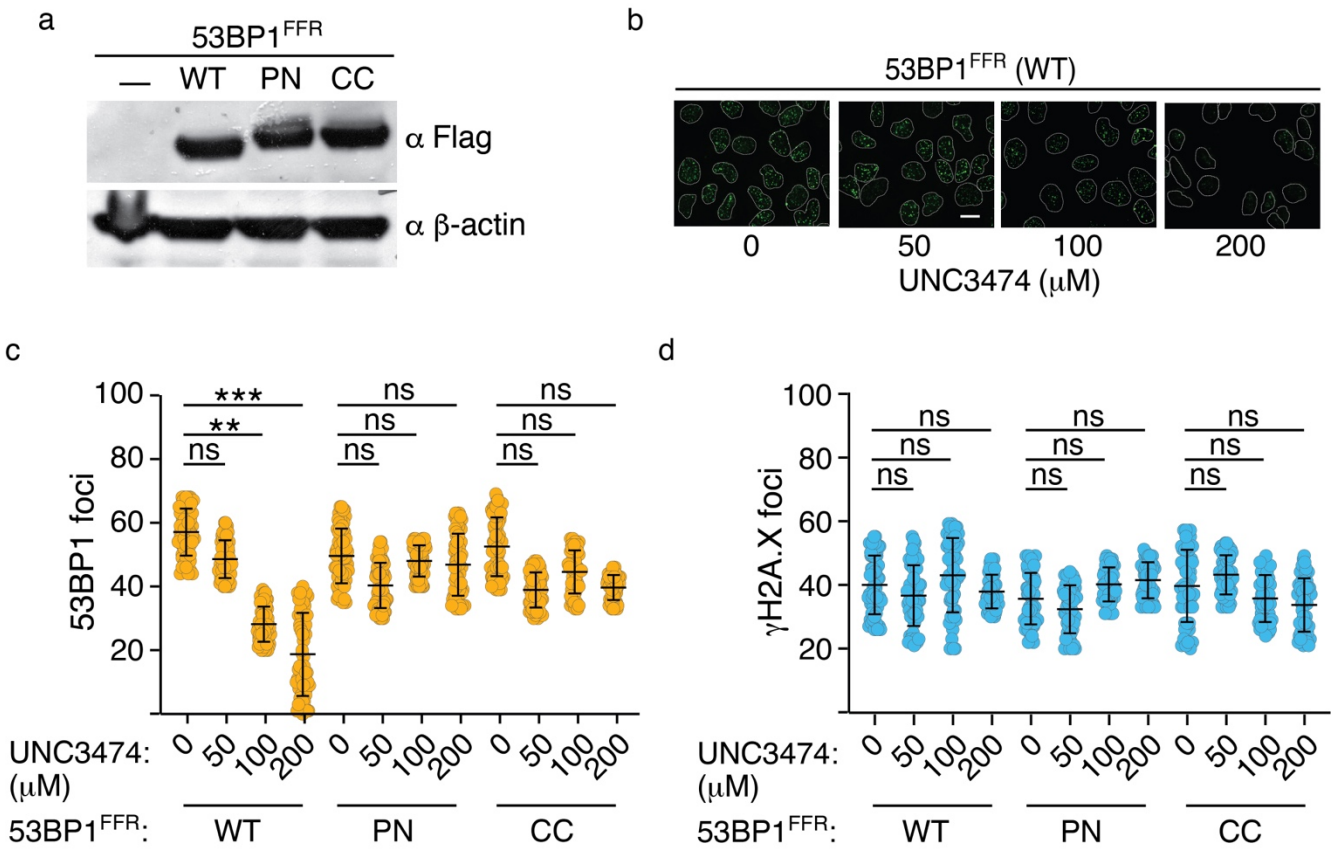

Figure 5 | Demonstration of an autoinhibited state for 53BP1 chromatin recruitment in cells using UNC3474 as a chemical probe.

a, Immunoblotting showing the expression of the indicated 53BP1^{FFR} construct in stably transfected U2OS cells. β-actin staining was used as control.

b, Representative data for the inhibition of 53BP1^{FFR} IRIF formation by UNC3474 after cell exposure to 1 Gy of X-ray radiation. Scale bar represents 10 μm.

c, Effect of UNC3474 on WT 53BP1^{FFR}, 53BP1^{FFR}-PN and 53BP1^{FFR}-CC IRIF number (mean ± s.d., n = 3).

d, Number of γH2A.X IRIF for the cells analyzed in **c** (mean ± s.d., n = 3). Labels *, ** and *** indicate $P < 0.05$, $P < 0.01$ and $P < 0.001$, respectively. P values were calculated using a two-tailed T-test. ns stands for not significant.

Table 1 Data collection and refinement statistics

	53BP1^{TT}-UNC2991 (PDB 6MXX)	53BP1^{TT}-UNC3351 (PDB 6MXY)	53BP1^{TT}-UNC3474 (PDB 6MXZ)	53BP1^{TT}-PN (PDB 6MY0)	53BP1^{TT}-CC (PDB 8FKH)
Data collection					
Space group	$P2_1\,2_1\,2_1$	$P3_121$	$P2_12_12_1$	$C2\,2\,2_1$	$P2_1\,2_1\,2_1$
Cell dimensions					
a, *b*, *c* (Å)	68.94, 159.43, 181.19	60.57, 60,57, 138.22	68.67, 160.71, 182.65	73.10,141.27, 47.06	72.50, 161.83, 179.95
α, β, γ (°)	90.00, 90.00, 90.00	90.00, 90.00, 120.00	90.00, 90.00, 90.00	90.00, 90.00, 90.00	90.00, 90.00, 90.00
Resolution (Å)	50-2.30 (2.38-2.30)*	50-1.62 (1.68-1.62)	50-2.50 (2.59-2.50)	50-2.20 (2.28-2.20)	50-3.79 (3.92-3.79)
R_{merge}	0.077 (1.06)	0.074 (0.741)	0.045 (0.436)	0.087 (0.55)	0.120 (0.621)
$I/\sigma I$	21.3 (1.3)	30.6 (2.7)	20.5 (2.4)	23.4 (5.3)	15.7 (3.2)
Completeness (%)	97.5 (75.3)	99.7 (98.0)	97.2 (76.4)	98.6 (87.4)	89.5 (75.1)
Redundancy	14.0 (6.7)	11.2 (8.0)	6.0 (6.1)	12.2 (11.4)	5.7 (5.0)
Refinement					
Resolution (Å)	48.14-2.30	18.48-1.62	17.60-2.50	39.60-2.20	48.19-3.79
No. of unique reflections	87459	37781	68884	12596	19548
R_{work} / R_{free}	0.21 / 0.23	0.18 / 0.21	0.19 / 0.22	0.19 / 0.23	0.28 / 0.33
No. atoms					
Protein	10054	1996	10562	1887	8405
Ligand/ion	297	46	221	129	
Water	411	348	667	240	
B-factors					
Protein	55.90	19.77	56.25	27.71	106.76
Ligand/ion	124.93	43.04	49.13		
Water	48.00	31.33	49.02	31.13	
R.m.s. deviations					
Bond lengths (Å)	0.004	0.019	0.003	0.004	0.004
Bond angles (°)	0.93	1.71	0.93	0.97	0.91

[a]Values in parentheses are for highest-resolution shell.

Supplementary Information

An autoinhibited state of 53BP1 revealed by chemical probes and protein engineering

Gaofeng Cui[1,*], Maria Victoria Botuyan[1,*], Pascal Drané[2,*], Qi Hu[1], Benoît Bragantini[1], James R. Thompson[3], David J. Schuller[4], Michael T. Perfetti[5], Lindsey I. James[5,6], Stephen V. Frye[5,6], Dipanjan Chowdhury[2] & Georges Mer[1,7,#]

*Equal contributions

[#]Correspondence: mer.georges@mayo.edu

Extended Data Figures

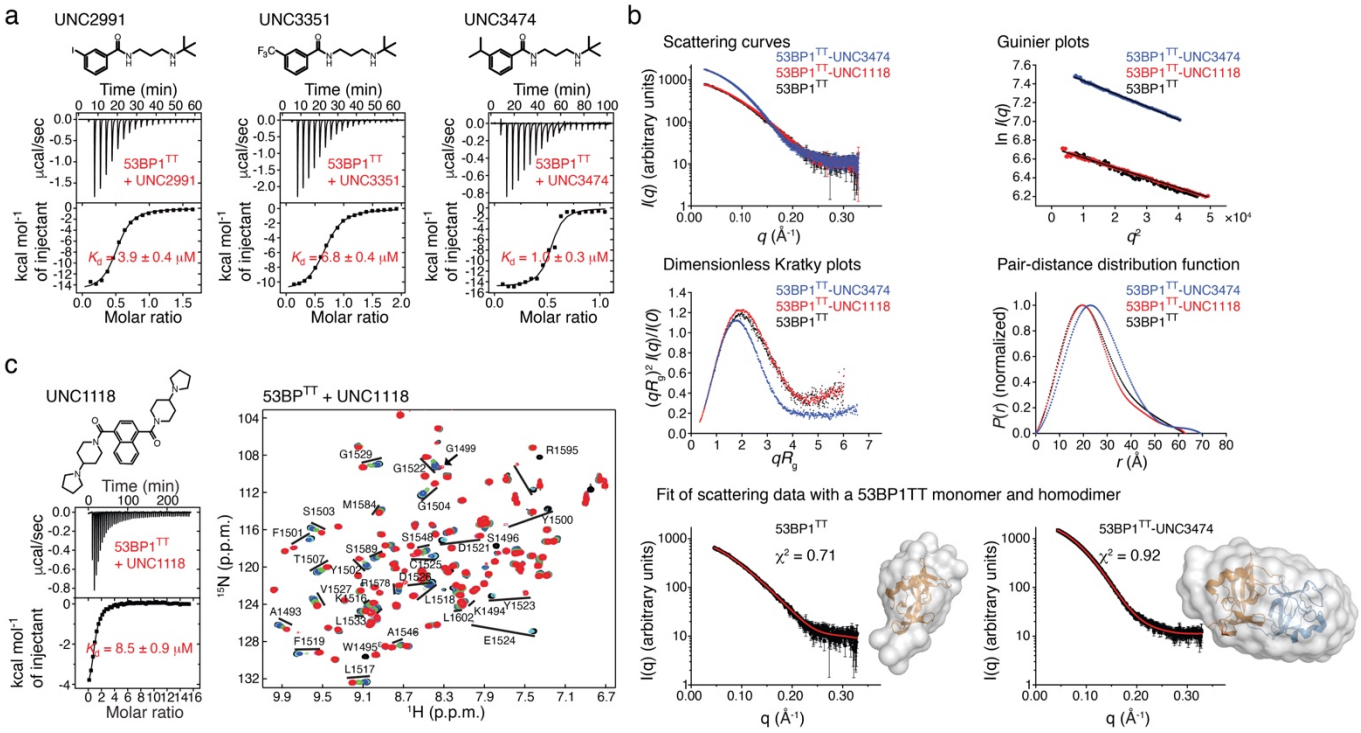

Extended Data Figure 1 | Interaction of 53BP1^{TT} with small molecules probed using isothermal titration calorimetry (ITC) and small-angle X-ray scattering (SAXS).

a, ITC of the interaction of UNC2991, UNC3351 and UNC3474 with 53BP1^{TT}. Raw titration data and integrated heat measurements are shown. Indicated apparent K_ds with associated standard deviations were determined by nonlinear least-squares analysis.

b, SAXS curves for 53BP1^{TT}, 53BP1^{TT}-UNC1118 and 53BP1^{TT}-UNC3474. Two mg/mL of 53BP1^{TT} was used, without and with 10-fold molar excess of UNC1118 or UNC3474. The Guinier plots, dimensionless Kratky plots and pair distance distribution functions derived from the SAXS data are shown. Also shown are the crystal structures of 53BP1^{TT} and 53BP1^{TT}-UNC3474 overlaid to the corresponding SAXS-based *ab initio* molecular envelopes generated using DAMMIF.

c, Interaction of UNC1118 with 53BP1^{TT} characterized using ITC (left) and NMR spectroscopy (right). For the ITC, raw titration data and integrated heat measurements are shown. The indicated K_d with associated standard deviation was determined by nonlinear least-squares analysis.

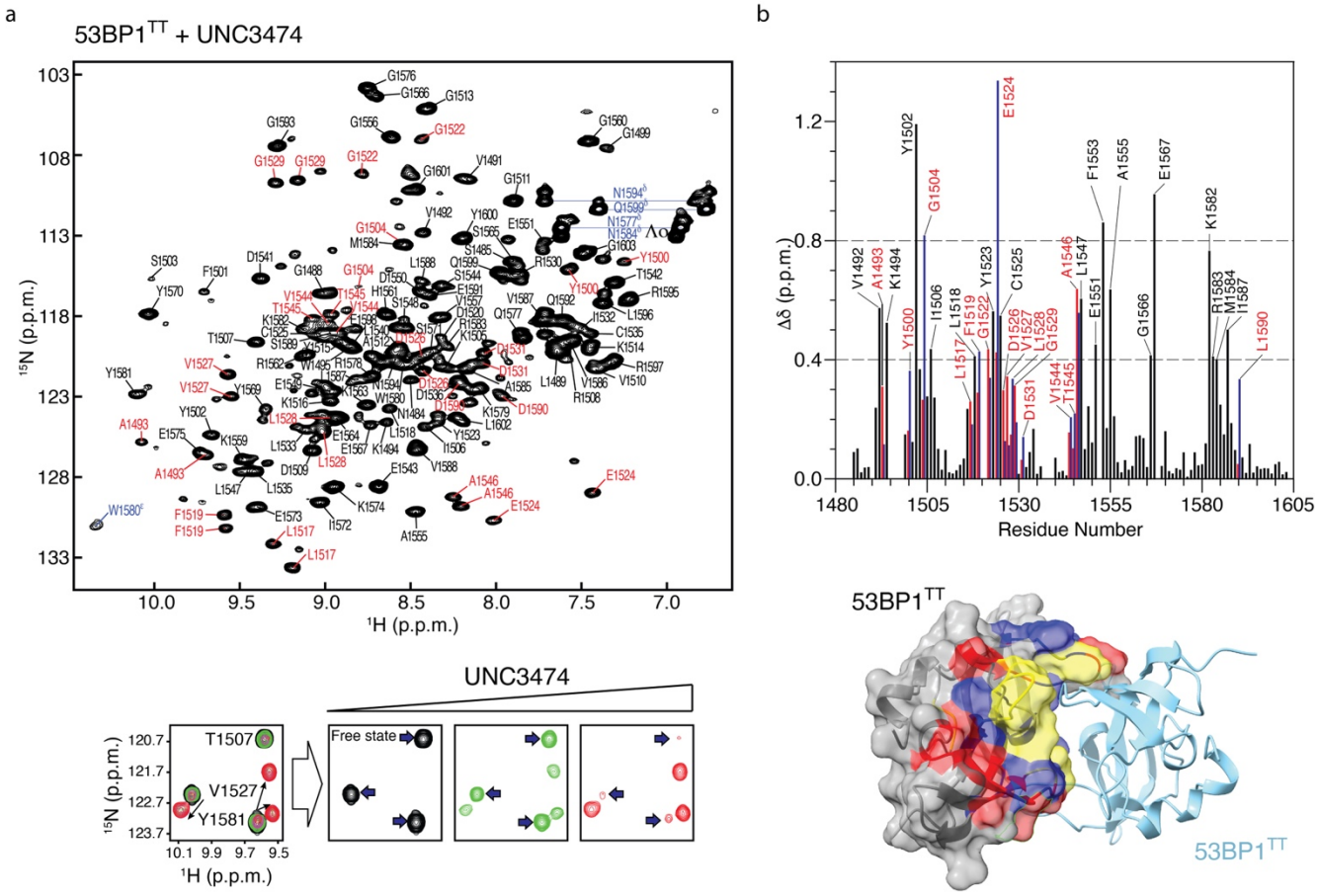

Extended Data Figure 2 | Interaction of 53BP1^{TT} with small molecules probed using NMR spectroscopy.

a, Top: Assigned ^{1}H-^{15}N HSQC spectrum of ^{15}N-labeled 53BP1^{TT} bound to non-labeled UNC3474 at a 53BP1^{TT}:UNC3474 molar ratio of 1:10. Residues for which there is doubling of resonances are labeled in red. The ^{1}H-^{15}N resonances for the asparagine and glutamine side chain amide groups and tryptophan indole ring are labeled in blue. Bottom: Changes in NMR signal positions for three residues in the ^{1}H-^{15}N HSQC spectrum of ^{15}N-labeled 53BP1^{TT} upon titration with non-labeled UNC3474 highlighting the slow exchange on the chemical shift time scale.

b, Top: Chemical shift perturbations ($\Delta\delta$) in ^{15}N-labeled 53BP1^{TT} at 10-fold molar excess of non-labeled UNC3474. Black bars are for residues with $\Delta\delta > 0.4$. Blue and red bars are for residues with split signals. Bottom: Mapping of chemical shift perturbations on the surface and ribbon representation of one of the two protomers in the 53BP1^{TT}-UNC3474 structure (UNC3474 omitted). Residues with $\Delta\delta > 0.4$ are colored blue and those with split signals are colored red. Residues for which signals are missing due to exchange broadening are colored yellow.

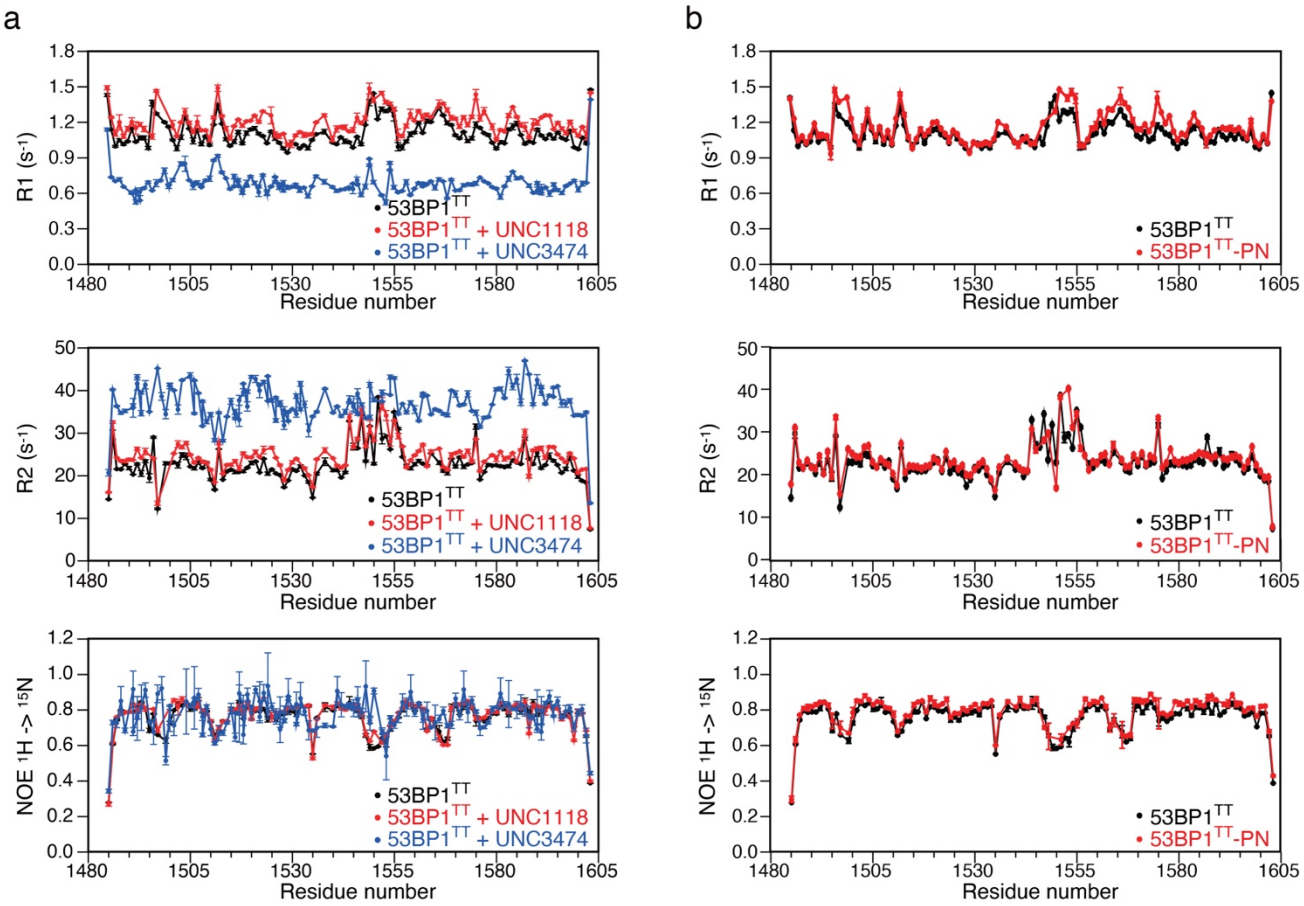

Extended Data Figure 3 | NMR relaxation measurements.

a, NMR relaxation values for 53BP1^{TT} without and with 9-fold molar excess each of UNC3474 and UNC1118.

b, NMR relaxation values for 53BP1^{TT} and 53BP1^{TT}-PN, both in free states.

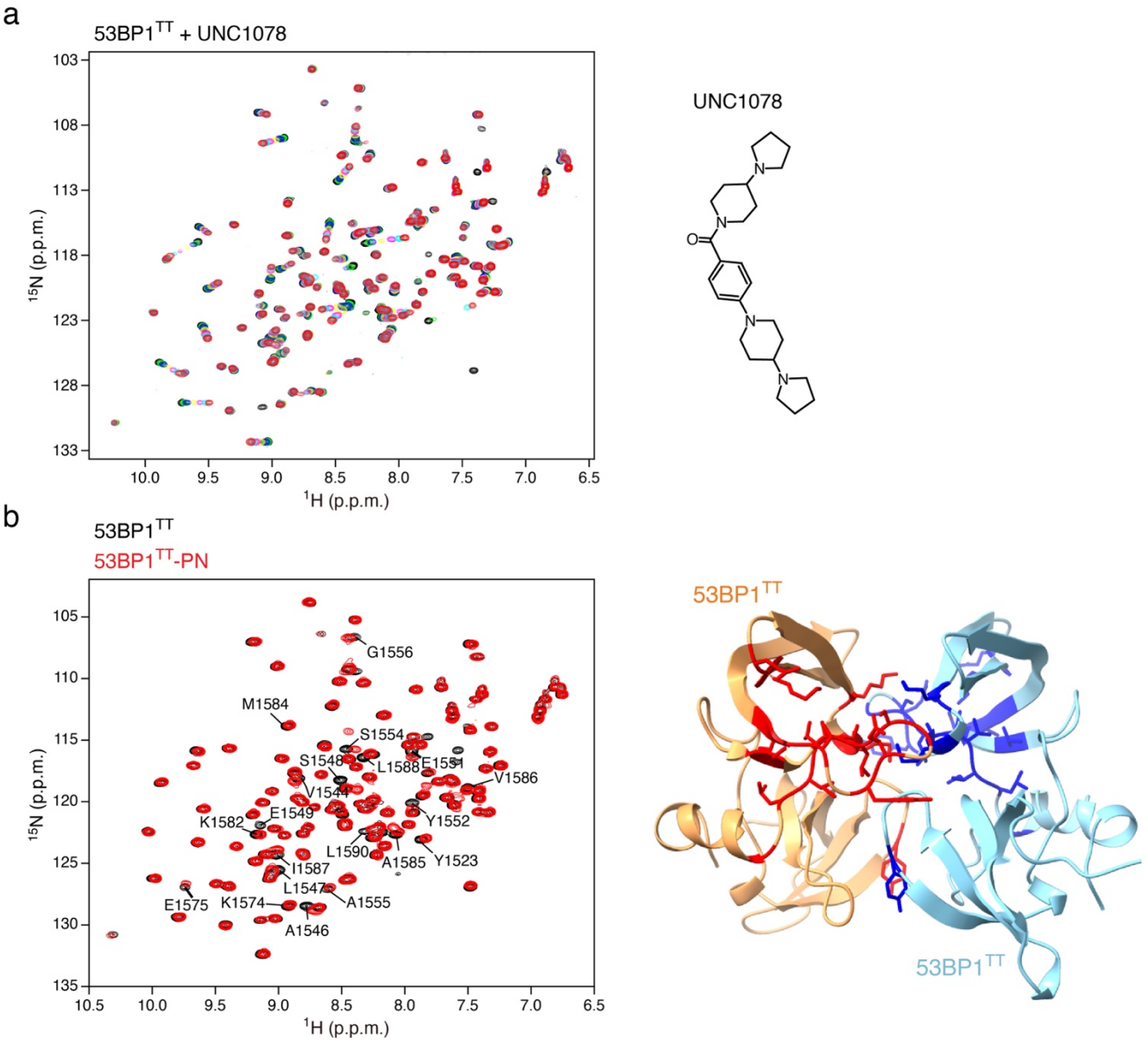

Extended Data Figure 4 | Comparative NMR spectroscopy of 53BP1^{TT} and 53BP1^{TT}-PN.

a, NMR spectroscopy-monitored interaction of 53BP1^{TT} with UNC1078. Shown in different colors are the overlaid ^{1}H-^{15}N HSQC spectra of 53BP1^{TT} recorded without (black) and with increasing amounts of UNC1078, up to 4-fold molar excess (red).

b, Overlay of the ^{1}H-^{15}N HSQC spectra of 53BP1^{TT} and 53BP1-^{TT}-PN. The two proteins were at a concentration of 0.3 mM. Residues for which the chemical shifts changed are labeled on the left. The residues are mapped (in red and blue colors) on the structure of the 53BP1^{TT} homodimer bound to UNC3474 (UNC3474 omitted) on the right.